MSc Report

The "fluid-mechanical sewing machine:"

State frequency analysis and parameter space mapping

Alex Cabaj

August 18, 2017

Abstract

When viscous fluid falls from a nozzle onto a moving horizontal belt, it forms a variety of patterns, which depend on the nozzle height and belt speed. This system is called the "fluid-mechanical sewing machine," and although it has been extensively studied, the frequency structures of many states have yet to be examined, and certain regions of parameter space remain unmapped. This report details the experimentally-derived frequency structures of previously unexamined states, and a few as-of-yet undocumented states are examined. Disordered states are also briefly examined, and states from a wide region of parameter space are sampled and classified.

Acknowledgements:

Contents

1   Introduction

When a viscous stream of fluid falls onto a flat, horizontal surface, it forms a coil.[1][2][3] This effect may be observed in everyday life with viscous fluids such as dribbling honey, and paint.[4] When rotational symmetry is broken by displacing the landing surface at a fixed velocity, the coiling is "unravelled", and a wide variety of states of motion is produced.[5]

This effect can be used in manufacturing, for example, in additive manufacturing, where coiling patterns finer than the resolution of the printing nozzle may be produced if the nozzle is moved at a particular speed at a particular height. In particular, the coiling effect can be used to produce foams [6] and hollow fibers [7].

The moving landing surface also allows for a more controlled lower boundary condition; the thread lands on a flat surface, instead of coiling onto itself in a column, as it does when the landing surface is immobile.[3]

Steady coiling motion has been shown in previous experiments to occur in four different regimes: the viscous (V) regime, the gravitational (G) regime, the inertio-gravitational regime (IG), and the inertial (I) regime; each regime is dictated by the relative magnitude of forces acting on the thread. The steady coiling frequency in the IG regime has been shown to be multi-valued. [1][2][3]

In this experiment, the control parameters of height H and belt speed U_0 were varied, while all other control parameters; namely, the flow rate Q, the nozzle diameter d, and the fluid properties (density ρ, and kinematic viscosity ν) were held fixed. Higher height ranges than those examined in [8] and [9] were explored, and a few previously-unobserved states were found. The frequency structure of these new states was examined. Additionally, the frequency structure of previously observed states whose frequency structure was not well-studied was also examined.

Dominant x and y frequencies of motion, along with their relative phases, were extracted from experimental results, and used as parameters for a kinematic model developed by

Brun et al[10] to successfully reproduce several observed periodic states. The previously unobserved periodic states were also successfully reconstructed by this model.

Finally, a preliminary examination of disordered states is also presented, followed by a brief discussion of experimental limitations, and buckling behaviour not accounted for in models of the motion.

2 Experiment

The experimental setup consists of a thread of silicone oil, which is emitted from a nozzle onto a moving conveyor belt. The setup used is similar to that used in [8] and [9]. The nozzle is made of stainless steel, and has a diameter of 8.00 ± 0.02 mm. A syringe pump (Harvard Apparatus PHD 2000) pumps the oil out of the nozzle at a fixed volumetric flow rate $Q = 1.635 \pm 0.005$ mL/min. A translation stage (Zaber T-LSR150B) allows for precise positioning of the nozzle at a height H above the belt, with a precision of $\pm 10^{-4}$ cm, although uncertainty in the zero height position of the nozzle increases this uncertainty to ± 0.01 cm. The belt is 16.0 ± 0.5 mm wide, and it is driven by a 50 000 step/rotation motor. The motor frequency is supplied by a computer-controlled signal generator. The belt speed, U_0, is adjustable to a precision of $\pm 10^{-3}$ cm/s. A scraper at the end of the belt scrapes off the excess oil for later re-use.

A mirror is placed at a 45°angle to the belt, which enables both the transverse and longitudinal motion of the thread (relative to the belt) to be captured by the camera. Following the convention used by [9], transverse motion is labelled x, and longitudinal motion is labelled y.

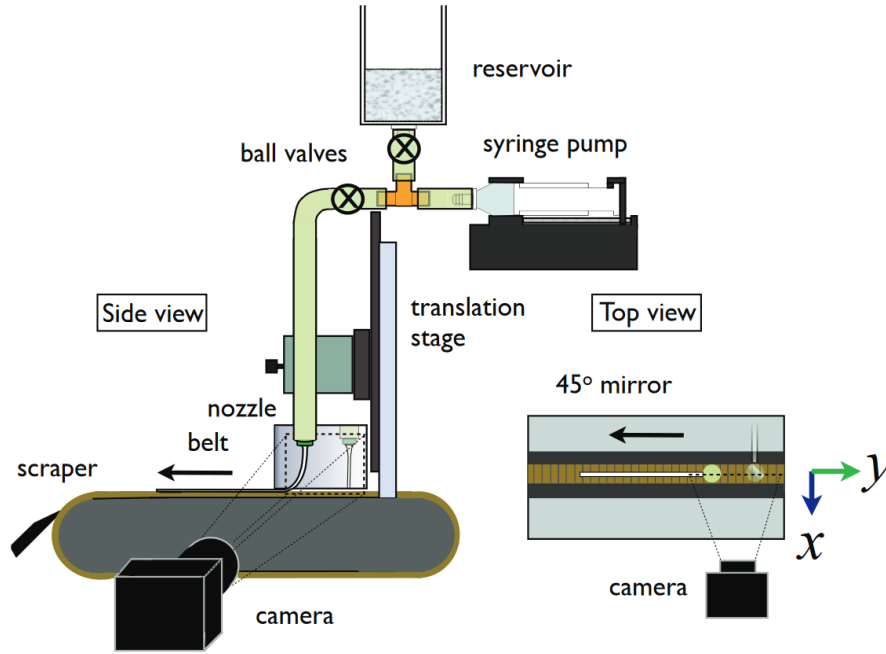A schematic of the experiment setup is shown in Figure 1.

Figure 1: Diagram of the experimental setup [9]

The fluid used in the experiment is 30 000 CSt silicone oil supplied by Sigma-Aldritch. It has a kinematic viscosity $\nu = 0.030 \pm 0.004$ m^2/s and a density of 0.9710 ± 0.0005 g/mL, both at 25°C. [11]

With this uncertainty in kinematic viscosity, the threshold value for the transition from the gravitational to the inertio-gravitational regime (as calculated based on nondimensional values given in [10]) ranges from $H = 5.0 - 6.0$ cm, and the threshold value for the transition from the inertio-gravitational to the inertial regime ranges from $H = 9.2 - 11.0$ cm.

Thus, most of this experiment is conducted in the IG regime, although parts of the I and G regimes are covered as well.

The experiment was run with a volumetric flow rate $\rho Q = 0.0270 \pm 0.0005$ g/s, which was verified by repeatedly weighing fluid collected from the nozzle over a short time period. No significant variation of the volumetric flow rate was observed over several measurements on different days. The choice of flow rate was motivated by Morris et al[8], who used the same flow rate with silicone oil having very similar properties to the fluid used in this experiment.

The experiment was conducted in several runs, each of which is detailed below in Table 1.

U_0 range (cm/s)	U_0 increment (cm/s)	H range (cm)	H increment (cm)	Temperature °C	Height above belt (mm)
2.50-5.00	0.50	7.00-12.00	0.50	25 ± 1	15 ± 1
5.50-8.00	0.50	7.00-12.00	0.50	25 ± 1	15 ± 1
3.00-3.80	0.10	6.50-8.50	0.50	21.9 ± 0.3	15 ± 1
2.60-2.90	0.10	6.00-7.50	0.10	23 ± 1	12 ± 1
1.70-1.75	0.05	5.00-8.00	0.10	24.0 ± 0.4	12.5 ± 0.5
1.70	-	6.00-8.00	0.10	23.9 ± 0.1	2.5 ± 0.5
13.30	-	8.50-10.00	0.10	24.4 ± 0.1	5.5 ± 0.5
13.30	-	9.50-12.00	0.10	24.4 ± 0.1	5.5 ± 0.5
4.00-4.10	0.10	6.50-12.00	0.10	23.9 ± 0.1	4.0 ± 0.5
2.50-3.50	0.50	6.50-12.00	0.50	23.7 ± 0.2	5.5 ± 0.5
4.00-5.50	0.50	6.50-12.00	0.50	24.1 ± 0.3	4.5 ± 0.5
6.00-7.50	0.50	6.50-12.00	0.50	23.4 ± 0.4	5.0 ± 0.5
7.00-7.20	0.10	6.50-8.00	0.10	23.7 ± 0.3	5.0 ± 0.5

Table 1: Table of runs. (All belt speeds are $\pm$ 0.01 cm/s, all heights are ±0.01 cm)

3 Data collection

The data was collected as a series of 3000 10-bit greyscale TIFF files with a size of 2351×100 px. The rate of image collection was 400 frames per second, resulting in 7.5 s of data per run. The camera height varied throughout the experiment; the heights of the segment of the frame above the belt from which the motion was extracted for each particular run are detailed in Table 1.

These heights were measured by photographing a calibration block with labelled 1-mm grid markings which sat flat on the belt. A photograph of this block is shown in Figure 2. Photographing the block would give an indication of height, and also allow for calculation of the number of px/mm to determine the measurement scale for the y position in plots. The same block was also photographed reflected in the mirror to find the scale for the x position.
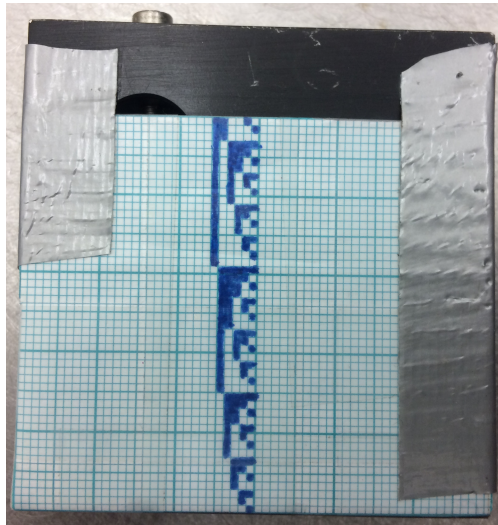

Figure 2: Calibration block; the grid has 1-mm spacing, and the dark blue markings indicate the height, in binary. (Binary numbers for height markings were used because the grid was too small to inscribe numeral markings.)

For each belt speed examined, the nozzle height was varied, first moving upwards to some given height, and then moving downwards, in order to examine possible hysteretic effects.

For each change of height and/or belt speed, there was a wait time of 6.000 ± 0.001 s between the adjustment and the start of image capture.

4   Image analysis

The images captured by the camera were 10-bit greyscale TIFF files with a size of 2351×100, saved as 16-bit images. Any given image has a brightness range from 0 to 1023.

In order to obtain the thread position at sub-pixel resolution, horizontal slices of the images were fitted to a model corresponding to the expected brightness for a transparent

thread. This allowed for information about the pixels surrounding the centre of the thread to be used to determine the thread's position, leading to a more accurate position result.

Each individual image was processed in the following manner.

First, a single horizontal line was chosen from the image; this is the height at which the position of the thread would be detected.

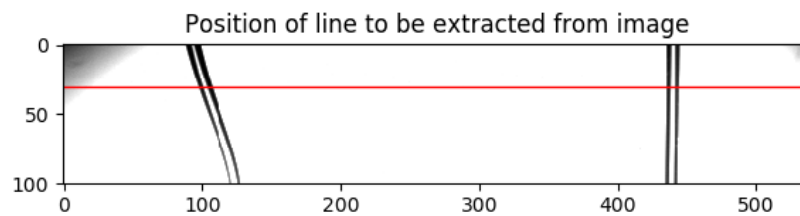Figure 3 shows an example of an image from which thread position would be extracted, with the chosen horizontal line indicated on the image.

Figure 3: Initial image

A line of brightness values was obtained. Figure 4 a) shows a plot of the brightness as a function of position along the line; note that troughs correspond to dark bands. The maximum brightness is 1023.

In order for a function modelling the brightness of light shining through a cylinder to be fitted to the thread, the approximate position of the thread would first need to be obtained. This was done by detecting the troughs using a first derivative.

First, the line was linearly interpolated and smoothed, in order to provide more points for the derivative to be performed, and to mitigate the effects of noise. A plot of the interpolated and smoothed line can be seen in Figure 4 b).

A first derivative of the line was taken, including only lines below a certain brightness threshold (to account for noise). A second derivative test was then used on regions where the sign of the first derivative changes in order to determine if the zero is at a minimum or at a maximum.

This would yield four points corresponding to the approximate locations of the minima,

8

which provide bounds for the edges of the strand. A plot showing the two strand edges detected for one strand is shown in Figure 4 c).
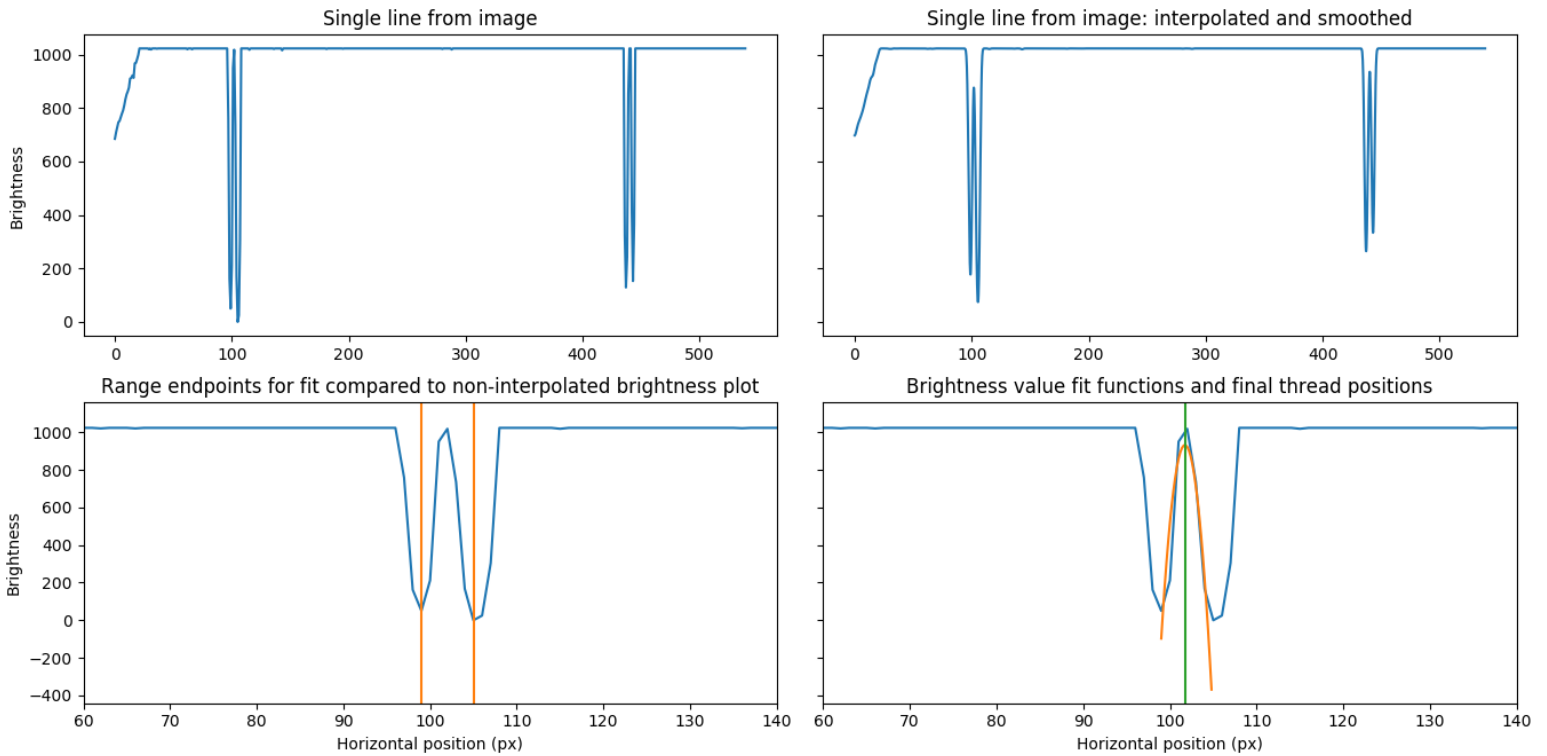

Figure 4: Edge detection process

Once the edges of the strands had been detected, a least-squares fit to a model function could be performed to obtain the strand positions. This fit was performed on the original data–not on the interpolated data–in order to avoid introducing any additional uncertainty. A plot of the model function fitted to one of the strands, along with the position extracted from the model, is shown in Figure 4 d).

Thus, a measurement of the thread position was obtained, to sub-pixel resolution. The final positions for the thread shown in Figure 3 is shown in Figure 5.
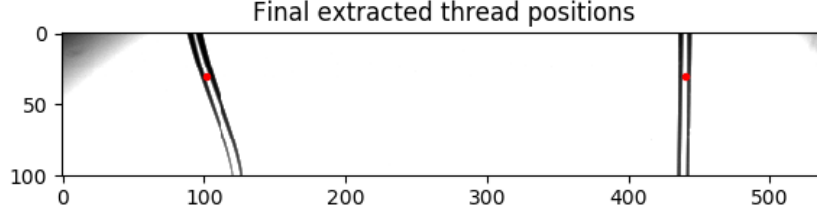
Figure 5: Final extracted positions

This process was repeated for all 3000 images of each run. If some of the data at the end of the run was unusable (due to the appearance of a bubble, for example), fewer images could be used to exclude images where the bubble was present. The presence of bubbles could be verified by visually examining the images.

5   Kinematic model for spectral signature reconstruction

Brun et al [10] demonstrated that several sewing machine patterns can be characterized in terms of magnitudes α_j, β_j, frequencies ω_j^x, ω_j^y, and phases ϕ_j^x, ϕ_j^y, and only a maximum of two frequencies are required for x and y respectively (i.e. $j \in \{1, 2\}$).

These parameters are used in the expressions

$$x(t) = \sum_{j \in \{1,2\}} \alpha_j \cos(\omega_j^x t + \phi_j^x) \tag{1}$$

$$y(t) = \sum_{j \in \{1,2\}} \beta_j \cos(\omega_j^y t + \phi_j^y) \tag{2}$$

which are referred to as a "kinematic model" by Brun et al. Together, these expressions reconstruct the x and y motion. Brun et al used parameters derived from the computational DVT method in this model.[10]. In a similar fashion, we will apply experimentally-derived parameters to the model and show that it successfully reproduces many of the experimentally-derived states.

6 Results

A diagram showing the region of parameter space traversed in the experiment is shown in
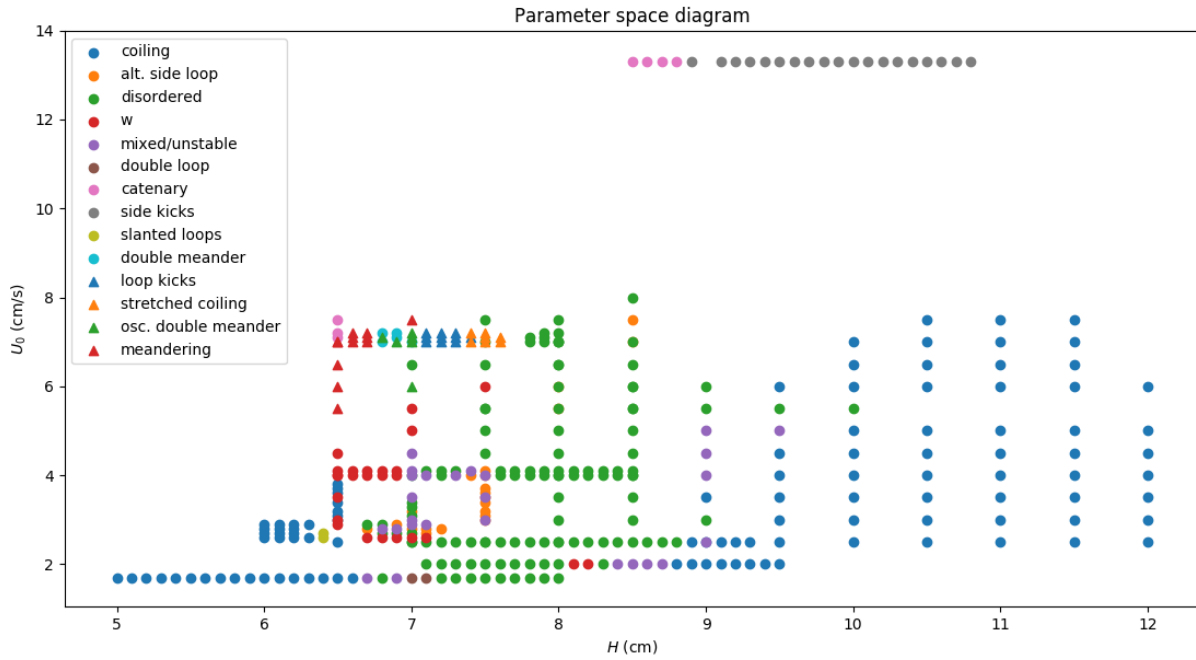Figure 6.

Figure 6: Parameter space

The states were classified based on their frequency spectra, and on visual examination
of the Lissajous plots and pattern reconstructions. Videos of the belt from above were also
used to visually confirm that the pattern reconstructions produced a faithful representation
of the belt pattern.

Table 2 shows a summary of the frequency ratios of the states observed.

State	ω_1^x	ω_2^x	ω_1^y	ω_2^y
Translated coiling	1	2	1	2
Double coiling	1	$\frac{1}{2}$	1	$\frac{1}{2}$
Loop kicks	$\frac{4}{3}$	$\frac{7}{3}$	1	2
Loop double kicks	$\frac{5}{4}$	$\frac{9}{4}$	1	2
Stretched coiling	1	2	1	2
Side kicks*	1	2	1	2

Table 2: Observed relative frequencies for states (ratio relative to dominant frequency)

7   States of interest

7.1   Double coiling

The double coiling state was observed experimentally by Chiu-Webster et al [5] and Morris et al [8], but the frequencies of the motion have yet to be examined in detail.

The observed double-coiling window was relatively small; as such, only a few double-coiling states could be examined.

The location of the double-coiling window in these results correlates closely with that found in [8]; the slight variation could be attributed to variations in temperature, or differences in fluid properties, since slightly different fluids were used.

A sample pattern reconstruction and Lissajous plot are shown in Figure 7.
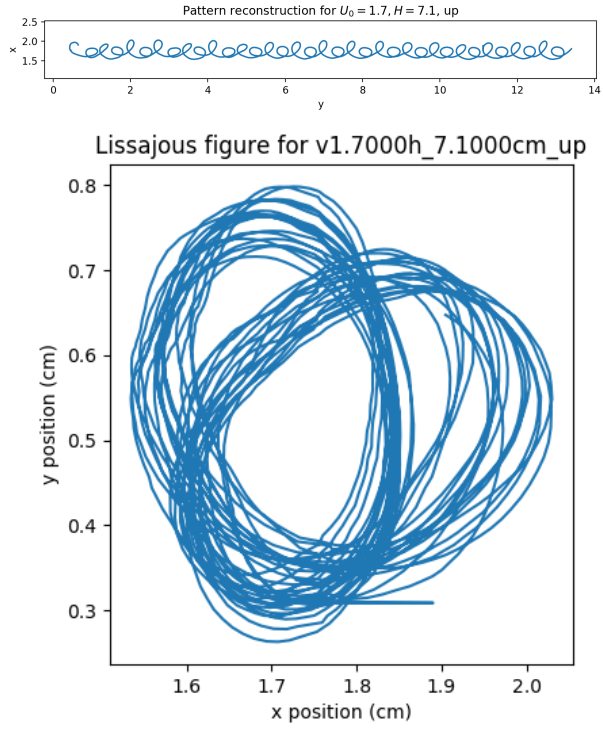
Figure 7: Double coiling: Pattern reconstruction and Lissajous plot

Translated coiling was also observed at heights slightly lower than the double coiling window; plots of this motion are shown in 8.
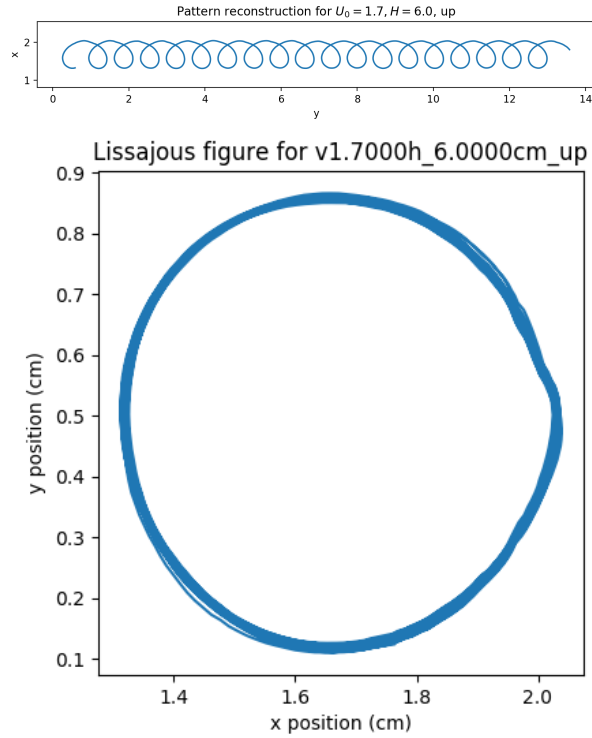
Figure 8: Translated coiling: Pattern reconstruction and Lissajous plot

A plot of the frequencies around the double coiling window as height is varied is shown in Figure 9. Generally, there is little variation of frequency vs. height in the coiling window. The green-shaded regions are regions of disordered behaviour; some of the frequency values are somewhat erratic due to a difficulty in pinpointing the peak frequencies of disordered motion. Note that in the double-coiling region, the dominant frequencies are reversed compared to the dominant frequencies in the coiling region.

14
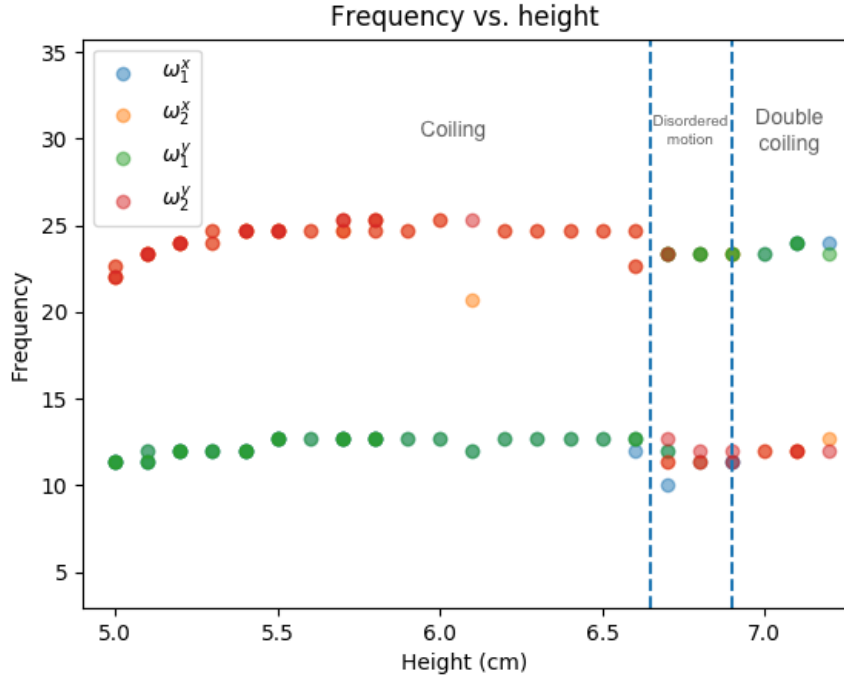
Figure 9: Frequency vs. height for region of parameter space around double coiling state. The windows delimited with dashed lines from left to right are: translated coiling, disordered motion, double coiling. The uncertainty in the frequencies is ± 0.1.

Furthermore, for the double coiling state, the two dominant frequencies are consistently in what is approximately a 2:1 ratio, with the highest-magnitude frequencies being twice the lowest-magnitude frequencies. This can be seen in Figure 10.
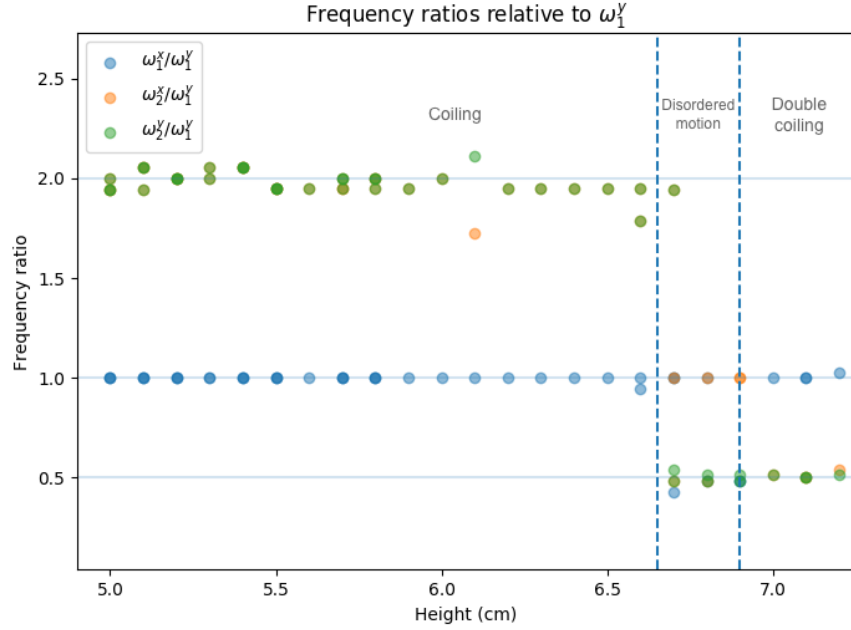
Figure 10: Frequency ratios for region of parameter space around double looping state. The windows delimited with dashed lines from left to right are: translated coiling, disordered motion, double looping. The ratios 2, 1, and 0.5 are indicated with horizontal lines for reference.

These results agree with the simulation conducted by Brun et al.[10] The kinematic model in Equations 1 and 2 also correctly reproduces the state given experimental values for frequency and phase. A reproduction of the Lissajous plot for the double-loop state using the kinematic model is shown below in Figure 11.

16
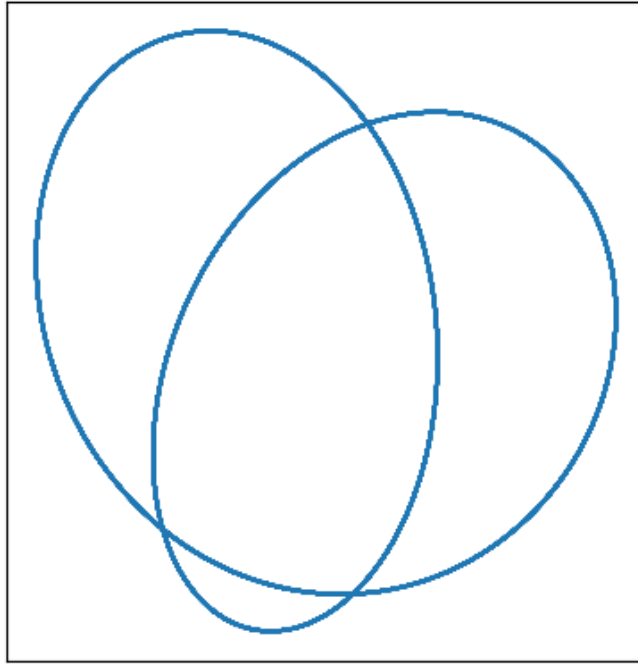
Figure 11: Double loop state constructed with the model in equations 1 and 2 using experimental frequency and phase values

7.2 Side kicks

Although the "side kick" pattern has been observed previously[5], no analysis of the frequency spectra of the motion of the thread in the side kick region of parameter space has been made.

Brun et al suggested that side-kick motion is a limiting case of stretched coiling.[10] The experimental results support this possibility, as will be discussed below.

No side-kick motion was detected during the cursory "broad" sweep of parameter space, and thus, the belt speed and nozzle height were manually adjusted until a clear side kick state was observed. Hence, the belt speed is considerably higher than the belt speed in all other runs.

Visually, the side-kick pattern consists of mostly straight lines, with regularly-spaced "kicks"; small perturbations in the x-direction.

By examination of the pattern formed on the belt, the side-kick motion appears to mostly

consist of the motion in the x-direction, (the "kicks" perpendicular to the belt motion). However, examination of the motion of the thread shows that the majority of the motion occurs in the y-direction in the "heel" of the thread, which exhibits a complex periodic oscillatory motion.

The x-motion is thus mostly undetectable, due to the low magnitude of the motion. Furthermore, effects of air currents pushing the thread in the direction transverse to the belt are also noticeable, and are of considerably higher magnitude than the x-motion itself. A Lissajous plot of a side-kick state is shown in Figure 12.
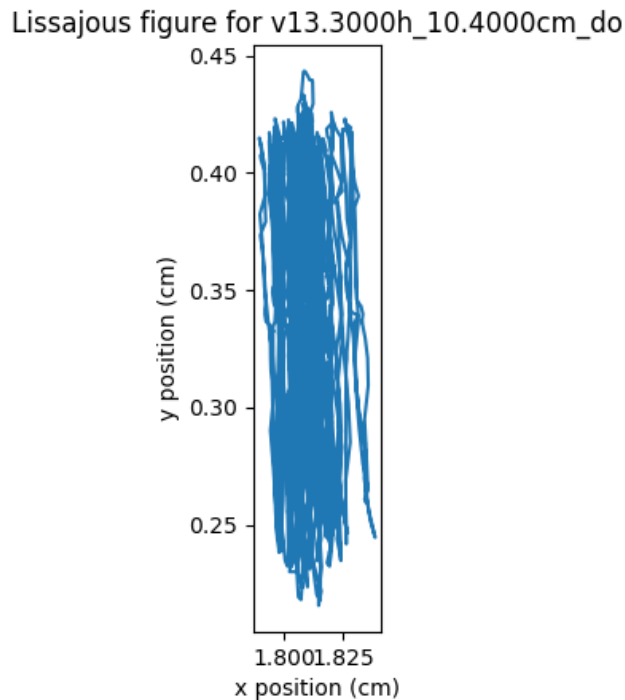
Figure 12: Lissajous plot of a side-kick state.

Despite the low magnitude of the x-direction motion, the position data for side kicks at a few heights had Fourier spectra for the x-direction with peaks large enough to detect, if lower frequencies were excluded (to account for the effects of air currents). Excluding these frequencies carries the risk that some information may be lost, if some of the lower-frequency signals are not due to air currents.

The assumption that lower x frequencies are negligible for certain heights was made based

on the magnitude of the dominant y-frequencies at those particular heights.

The parameters extracted from the motion were used with the model to generate patterns based on the most dominant frequencies.

The x and y Fourier spectra corresponding to a state which had relatively large peaks in the x frequencies are shown in Figure 13. Also shown is the pattern constructed by using the experimentally extracted frequency values from the above spectra with the kinematic model.
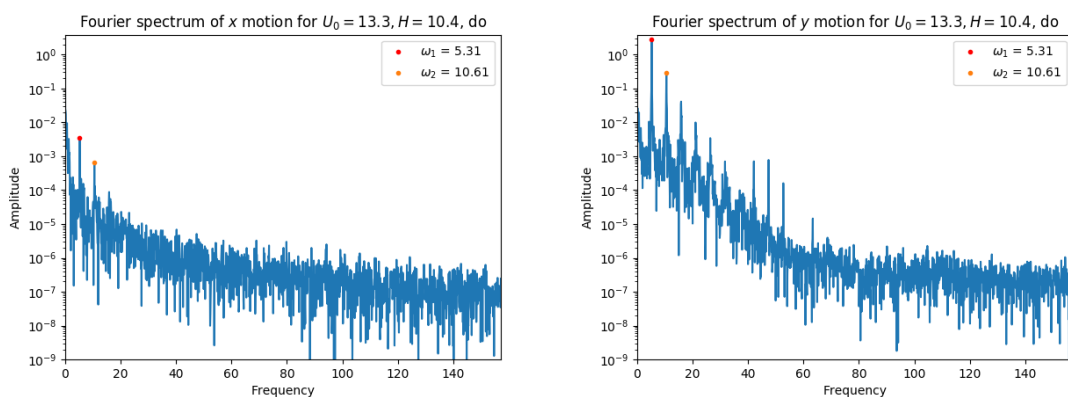

Figure 13: Side kicks: Fourier spectra, with corresponding reconstruction from model (not to scale)

The reconstructed pattern appears to resemble double meander motion, albeit with an extremely small amplitude in the x-direction.

However, video observations suggest that the motion is not meandering, but instead involves some overlapping of the thread. This is consistent with the assumption that the motion can be considered the limit of stretched coiling as the extent in x becomes very small

compared to the y motion.[10] The agreement in frequency ratios supports this, as seen in Table 2.

Snapshots of the motion from the camera can be observed in Figure 14.
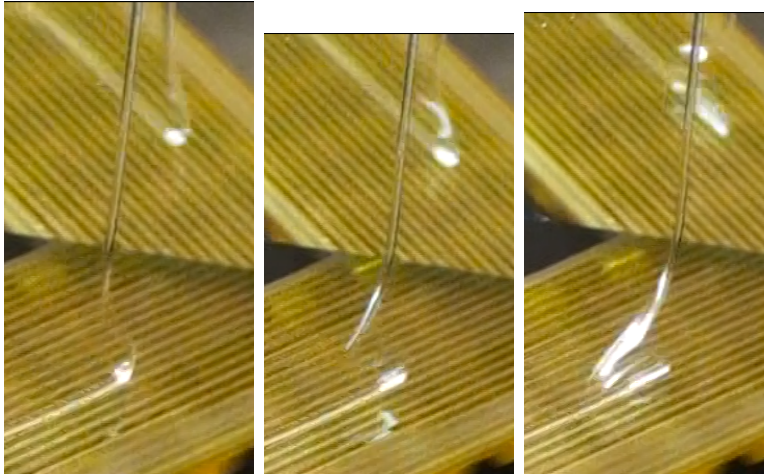
Figure 14: Sequential stills from camcorder footage of side kick motion. Note the bending and buckling of the thread. The images are blurred due to the high speed of the motion compared to the low framerate of the camcorder.

Although the amplitude of the x motion is difficult to resolve, the movements of the heel of the thread in the y-direction are distinctly periodic, and have a relatively large amplitude.

A plot of frequency vs. height for the y-component of the motion of all the side kick states observed is shown below.
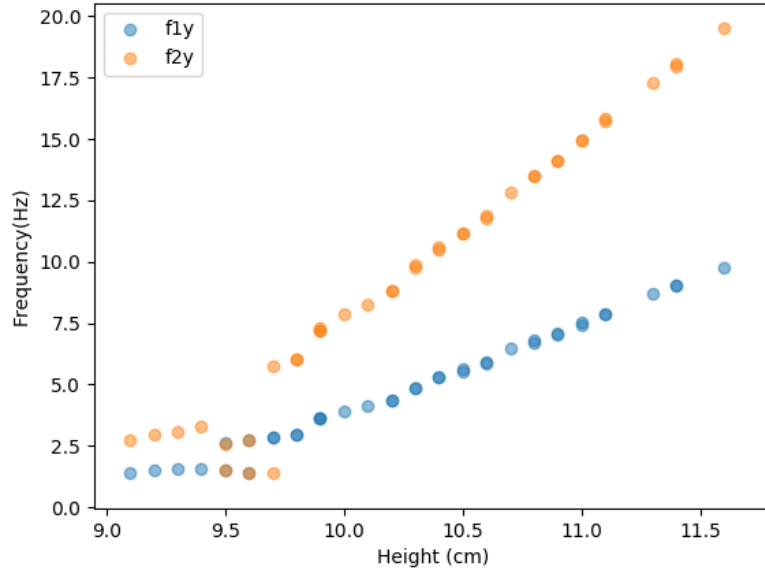
Figure 15: Frequency vs. height for region of parameter space around side kick state. The uncertainty in the frequencies is ± 0.1.

In general, the frequencies increase with height, except in a small region around $H = 9.6$. Aside from the aforementioned region around $H = 9.6$, the ratio of ω_1^y to ω_2^y is 2, as shown in Figure 16.
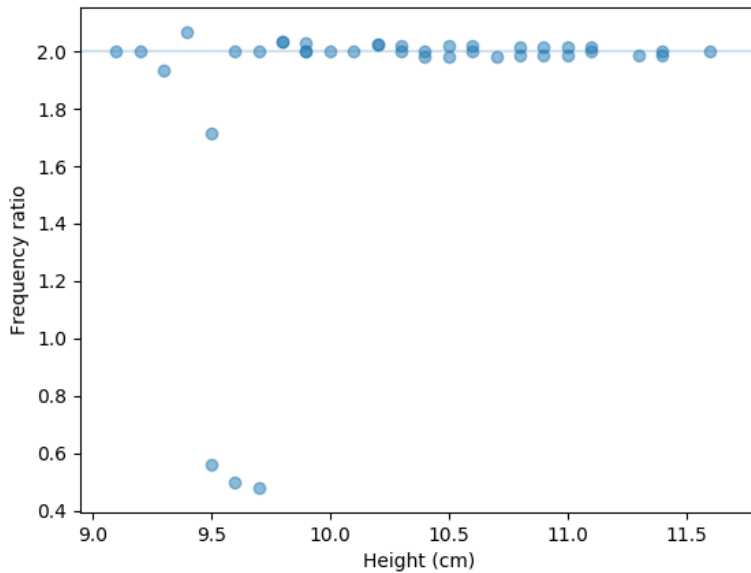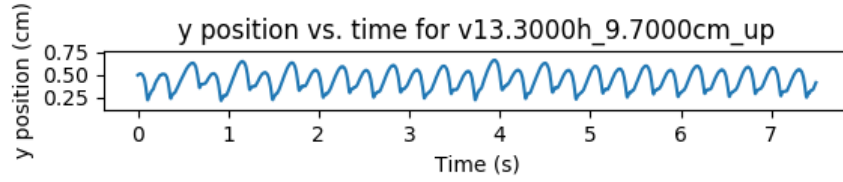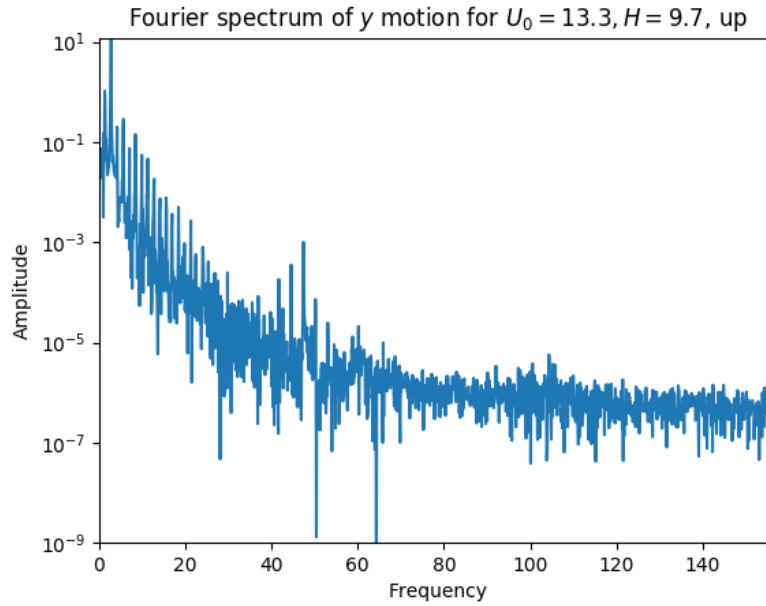
Figure 16: Frequency ratio vs. height for side kick motion. The line $y = 2$ is plotted for reference

The dip in frequency ratios around $H = 9.6$ is accompanied by more complex motion in the y direction. A plot of this y motion and its corresponding frequency spectrum is shown in Figure 17

(a) y motion vs. time

(b) Spectrum of y motion

Figure 17: Side kick motion

Given that the range for the critical height value separating the inertio-gravitational and inertial regimes is $9.2 - 11.0$ cm, it is possible that the range $H = 9.5 - 9.7$ is still in the IG regime. The steady coiling frequency in the IG regime is multi-valued, which could explain the variation in frequency.[3] Above $H = 9.2 - 11.0$ cm, the frequency is single-valued, which is consistent with the single-valued steady coiling frequency in the I regime.

A plot of simpler y-motion at a higher height, the same motion whose frequency spectrum is shown in Figure 13, is shown below in Figure 18 for comparison.

23
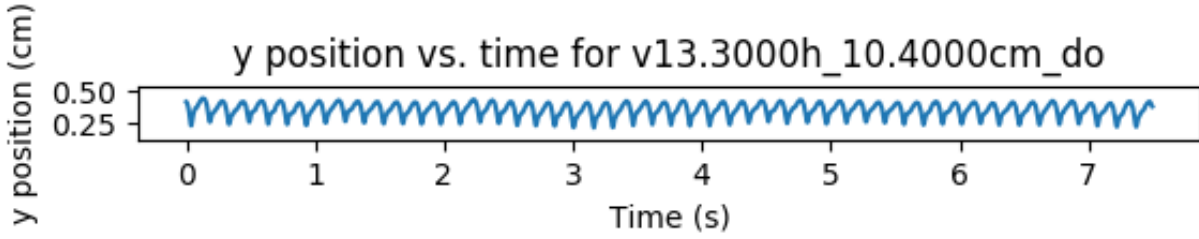
Figure 18: Side kicks: y motion vs. time

The x motion at the height with the more complicated pattern cannot be resolved, and as such, it is not possible to reconstruct the entire pattern, or to generate the pattern with the model. Further observation is necessary in order to examine this motion in more detail.
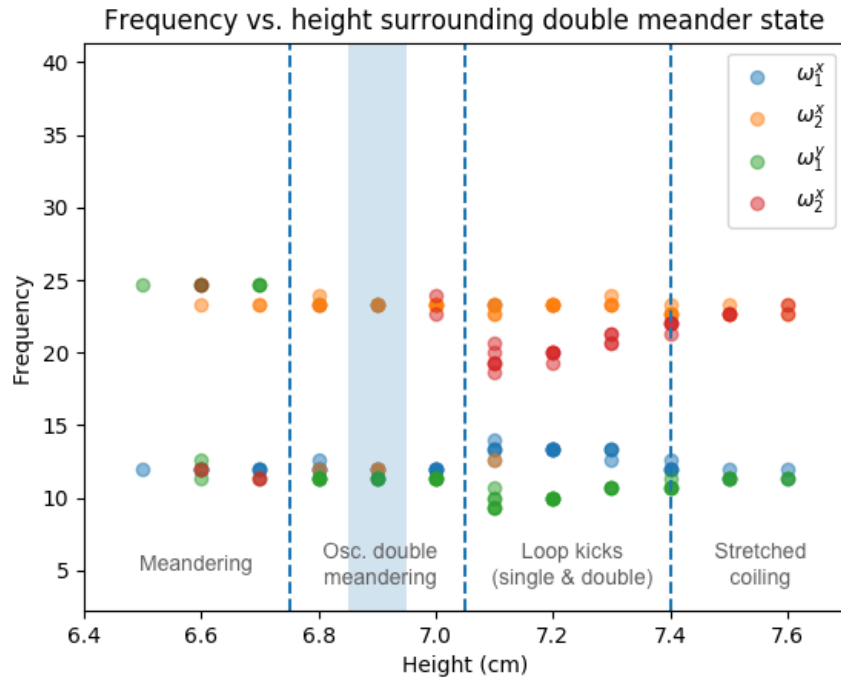
8 Double meandering window

Figure 19: Frequency vs. height for region of parameter space around double meandering state. The uncertainty in the frequencies is ± 0.1. The region containing states most resembling pure double meandering is shaded in blue. The windows divided by dotted lines are, from left to right: meandering, oscillatory double meandering, loop (single and double) kicks, and stretched coiling. Frequencies with amplitudes too low to resolve are excluded.
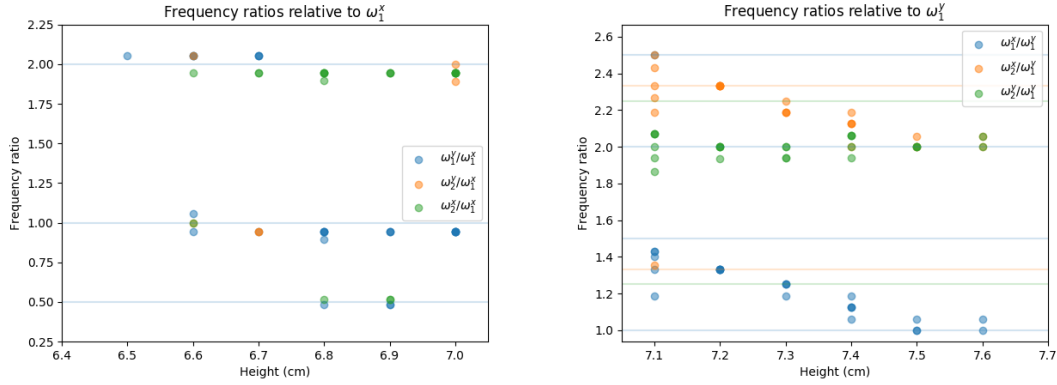
Figure 20: Frequency ratios for double meandering window, relative to the frequency component with highest amplitude. The frequency ω_1^x dominates for $H \leq 7.0$ cm, whereas the frequency ω_1^y dominates for $H \geq 7.1$ cm. Horizontal orange and green lines in the ω_1^y plot correspond to the ratios for the loop kicks and loop double kicks, respectively.
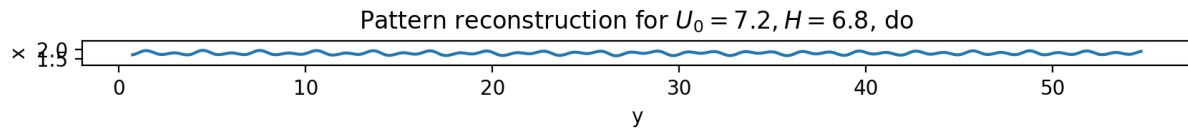
8.1 Double meanders

The "double meander" state was observed by [8] in a region of parameter space around heights of H_0= 7.2-7.4 cm, and around belt speeds of $U_0 = 6$-8 cm/s.

This region was investigated in more detail in this experiment, for belt speeds ranging from 7.0-7.2 cm/s. Some states resembling double-meander motion and displaying phase relationships similar to those described in [10] were observed.

Brun et al characterize the double-meander state as having relationships between the frequencies as follows: $\omega_1^x = \omega_1^y = \omega_2^x/2 = \omega_2^y/2$.[10].

None of the motion observed in this run consisted of pure double meanders. Instead, a quasi-periodic state similar in appearance to double meandering, except that the double meanders appear to gradually switch sides, being modulated by a sinusoidal curve.

A sampling of these patterns is shown below in Figure 21. Figure 21a displays one of the patterns more closely resembling pure double meander motion.
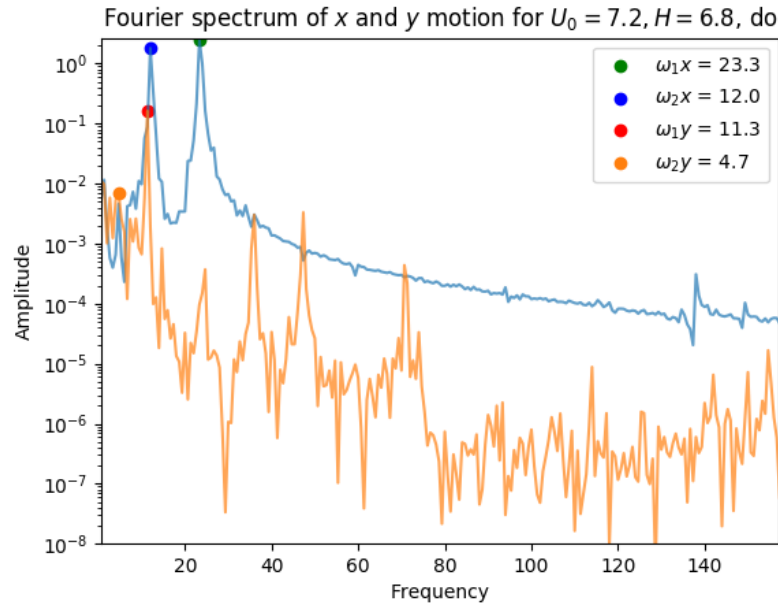
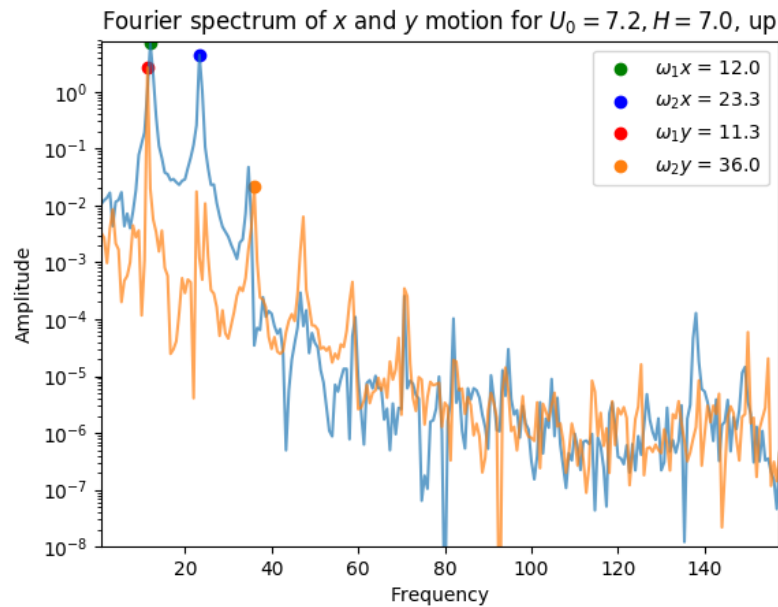(a) Double meanders (with relatively minimal oscillation)
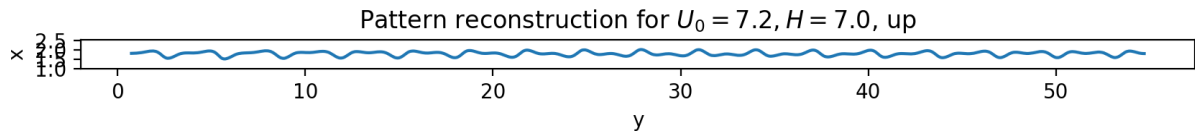
(b) Oscillatory double meanders

Figure 21: Double meander motion

An examination of videos taken from above the belt reveals that these patterns agree well with the pattern formed on the belt.

(a) Double meanders (with relatively minimal oscillation)

(b) Oscillatory double meanders

Figure 22: Frequency spectra for double meander motion. The x spectrum is in blue, and the y spectrum is in orange.

Figure 22a shows the frequency spectrum for the double meander motion reconstructed in Figure21a; the frequency spectrum corresponds fairly well with results from the DVT

simulation in [10], although it differs due to its strong ω_2^x component, which is not present in the simulation results.

Conversely, in the frequency spectrum for the oscillatory double meander motion ω_1^x has a considerably higher amplitude than ω_2^x and ω_1^y. The magnitude of ω_2^y is still negligible. The relatively high amplitude of ω_2^x is responsible for the oscillation.

The frequency ratios observed for the oscillatory double meander motion are documented in Figure 20.

Assuming that only the ω_1 and ω_2 frequency components are significant in x and y, whether or not the oscillatory double meander motion is periodic depends on whether or not the ratio of the x and y frequencies is rational. The motion in x and y are periodic when considered independently of each other, but if the ratio between the frequencies in x and y is irrational, then the motion may be periodic in x and y independently, while being aperiodic overall.
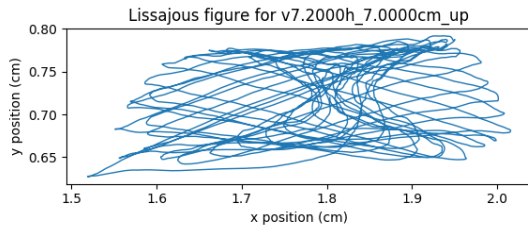
Comparisons between Lissajous plots of the observed motion and the reproduction from the model in equations 1 and 2 are shown in Figure 24. The kinematic model faithfully reproduces the motion.
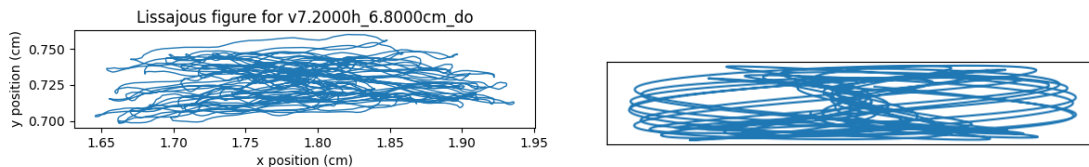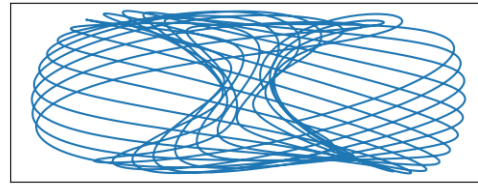

(a) Double meander: observed   (b) Double meander: model

Figure 23: Double meander: reconstructed pattern vs. model

(a) Oscillatory double meander   (b) Oscillatory double meander: model

Figure 24: Oscillatory double meander: reconstructed pattern vs. model

8.2 Loop kicks

A set of new, previously undocumented states was observed in the regions between $H = 7.1$ and $H = 7.4$ for $U_0 = 7.0, 7.1, 7.2$.

These states consist of alternating side loops, interspersed with regular "kicks".

Two different patterns of kicks have been observed: one alternates loops with kicks, and the other has a repeating pattern of two alternating side loops followed by a kick.

Both states are stable, but are subject to hysteretic effects.

Despite the apparent complexity of the motion, the kinematic model in Equations 1 and 2 is able to reproduce these states, when given experimental parameters, and only the two dominant frequencies are required in the x and y directions. A comparison of the experimental and reproduced plots is shown.

Figures 25 and 26 show the two different loop kick patterns reconstructed directly from observations, compared to constructions of the patterns from the model itself. There is re-markable agreement between the patterns. Furthermore, the reconstruction from the model manages to capture the actual loops in the thread, contrary to the reconstruction, since the pattern is reconstructed from a point on the thread slightly above the belt. (In this case, at a height of 5.0 mm ± 0.3 mm above the belt.)
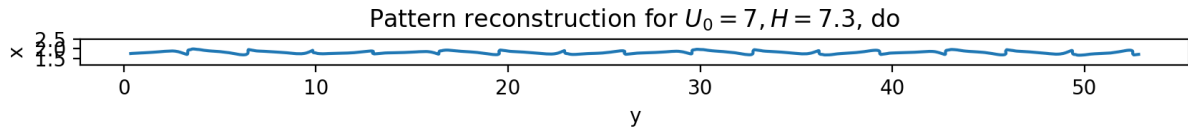
Pattern reconstruction for $U_0 = 7, H = 7.2$, up
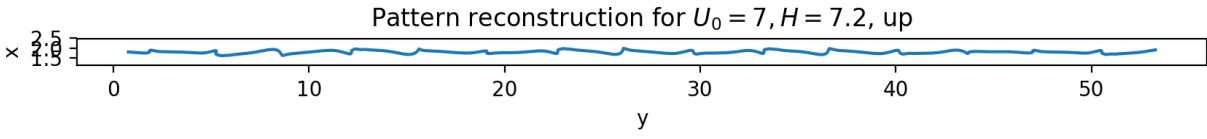
(a) Loop kicks

(b) Loop kicks: model

Figure 25: Loop kicks: Reconstructed pattern vs. model

Pattern reconstruction for $U_0 = 7, H = 7.3$, do
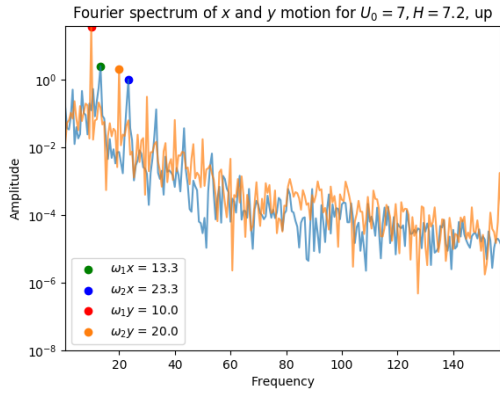
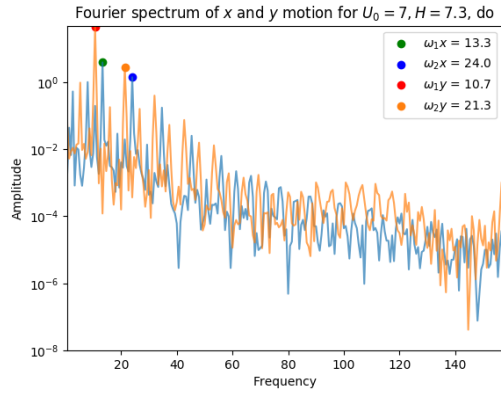(a) Loop double kicks

(b) Loop double kicks: model

Figure 26: Loop double kicks: Reconstructed pattern vs. model

The frequency spectra of the loop kick and double-kick patterns resemble those of the alternate-side-loop state, as documented in [10], albeit with a somewhat different frequency ratio. The frequency spectra of the patterns in Figures 25 and 26 are shown below in Figure 27, and the corresponding frequency ratios are listed in Table 2.
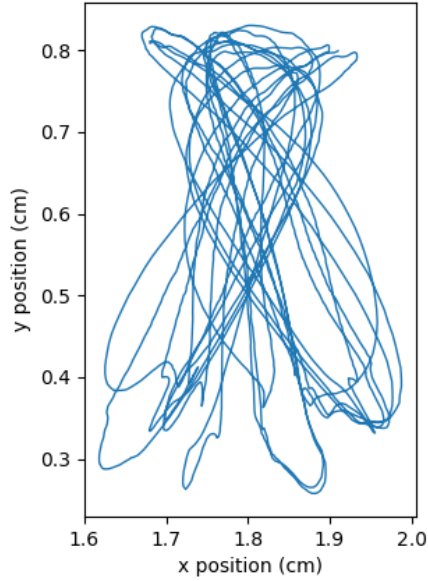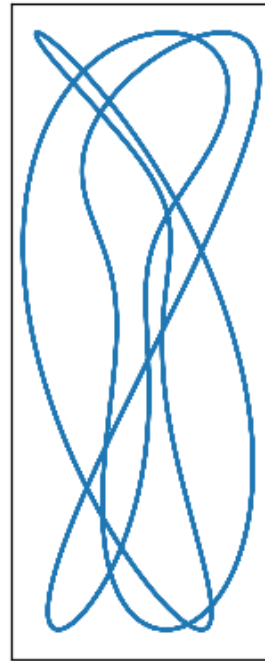
(a) Loop kicks

(b) Loop double kicks

Figure 27: Loop kicks and loop double kicks: Frequency spectra

The Lissajous plots generated from the model show good agreement with experimental results, and highlight the periodic motion of these states.

(a) Loop kicks

(b) Loop kicks: model

Figure 28: Loop kicks: reconstructed pattern vs. model
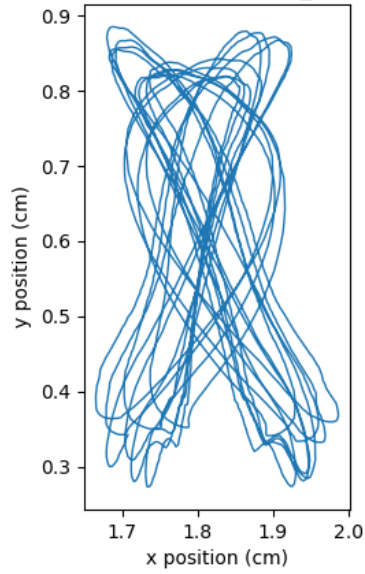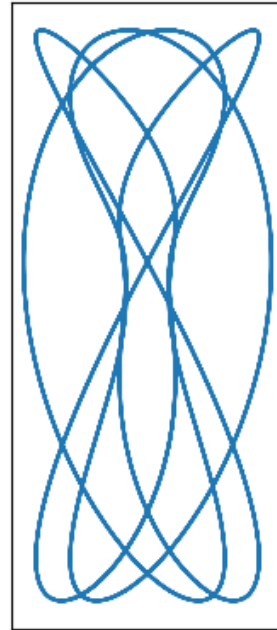
(a) Loop double kicks (b) Loop double kicks: model

Figure 29: Loop double kicks: reconstructed pattern vs. model

8.3 Stretched coiling

Just above the loop kick window, a small window of stretched coiling can be found. This strethced coiling was observed in a similar region of parameter space by Morris et al.[8]

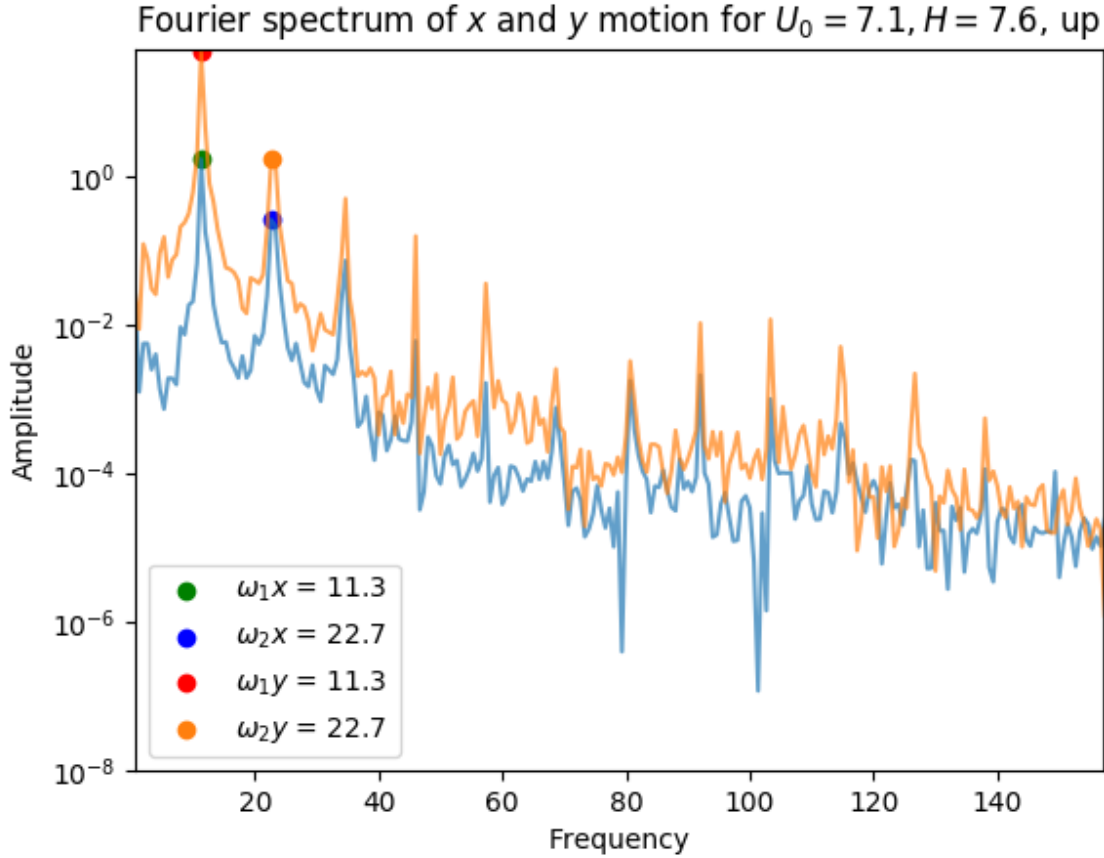The frequency spectrum of this motion may be found below.

Figure 30: Stretched coiling: spectrum

The stretched coiling pattern emerges as the frequencies ω_1^x and ω_1^y approach each other, and likewise, as the frequencies in ω_2^x and ω_2^y approach each other, as can be seen in figure 19. The frequency ratios approach 2:1 for the first and second dominant frequencies in both x and y.

This agrees with the frequency ratio predictions in [10].

The state can be recreated using the kinematic model, although there is a 'kick' in the Lissajous plot around (1.8,0.4) which does not appear in the model. Further investigation is necessary to verify whether or not this is a feature which appears on the belt, or whether the 'kick' is caused by motion higher up along the strand which does not appear on the belt.

Lissajous figure for v7.1000h_7.6000cm_up

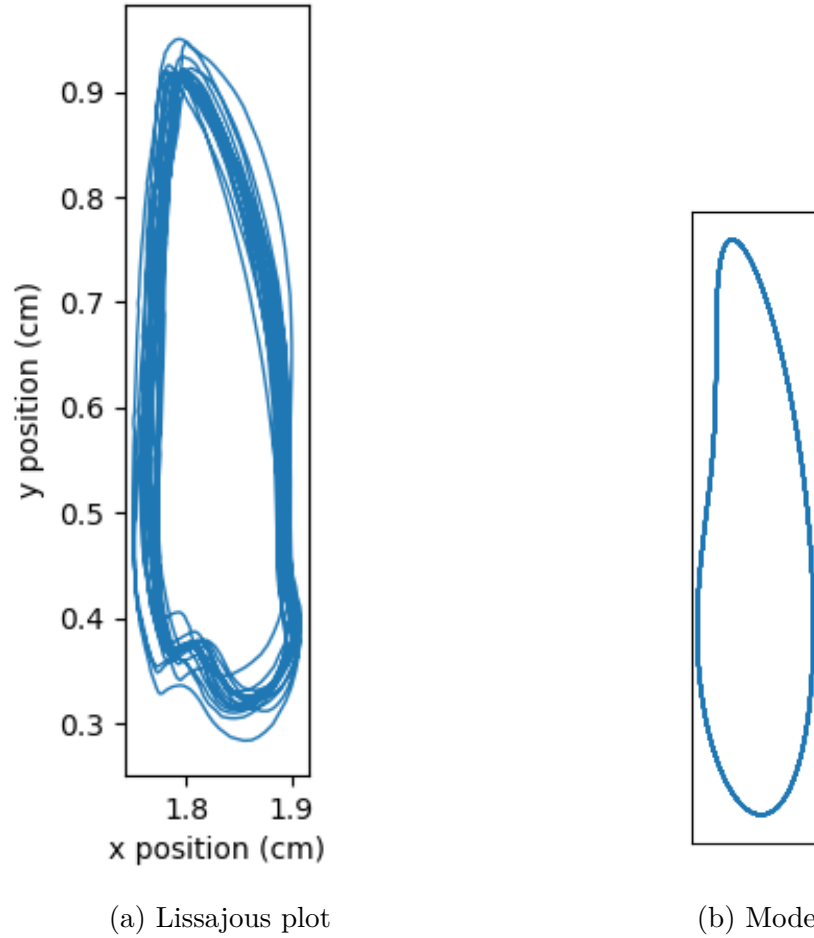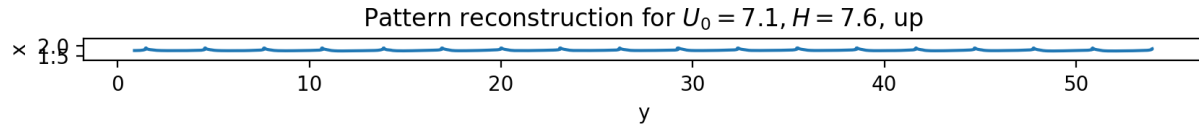(a) Lissajous plot   (b) Model

Figure 31: Stretched coiling: Lissajous plot vs. model

Below, in Figure 32 is a comparison between the pattern reconstruction of stretched coiling with the model. Note that despite the missing 'kick' in the Lissajous plots, the experimental reconstruction and the model are very similar in appearance.

(a) Stretched coiling: reconstruction

(b) Stretched coiling: model

Figure 32: Stretched coiling: reconstructed pattern vs. model

8.4 Disordered motion

Disordered motion was observed in several regions of parameter space. In particular, one window of disordered motion was present at heights above the stretched coiling window. This disordered motion was not observed to settle into a periodic state after several oscillations, and appears to exhibit irregular motion for an indefinite period of time.

The reconstructed pattern, Lissajous plot, and frequency spectrum of the disordered motion above the stretched coiling window may be found below in Figure 33.
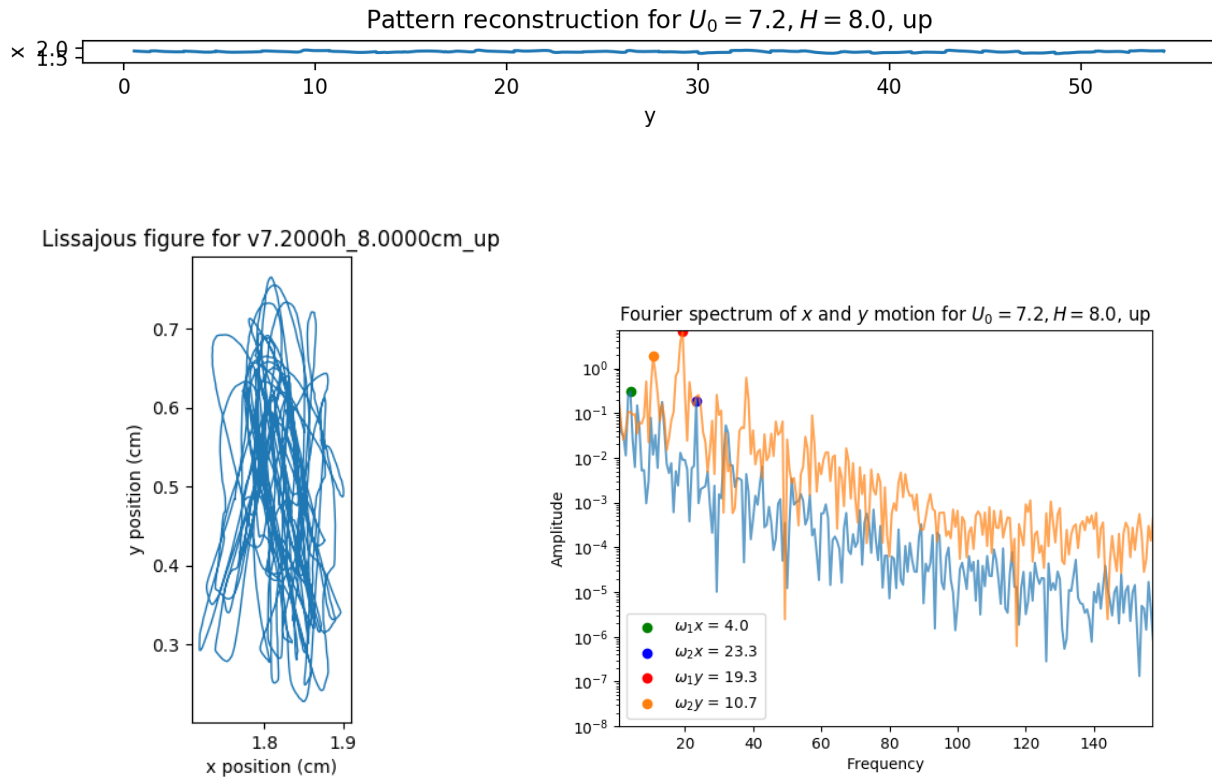
Figure 33: Disordered motion: pattern reconstruction, Lissajous plot, and frequency spectrum

In their observations of disordered motion, Chiu-Webster et al[5] claim that it can be described as "an apparently random sequence of side kicks, meanders and figures-of-eight". Results from this current experiment algree with Chiu-Webster et al's observations, as can be seen in the pattern reconstruction.

Another example of this sort of disordered motion in a different region of parameter space, where the amplitude of the x motion is higher, is shown for reference in Figure 34.
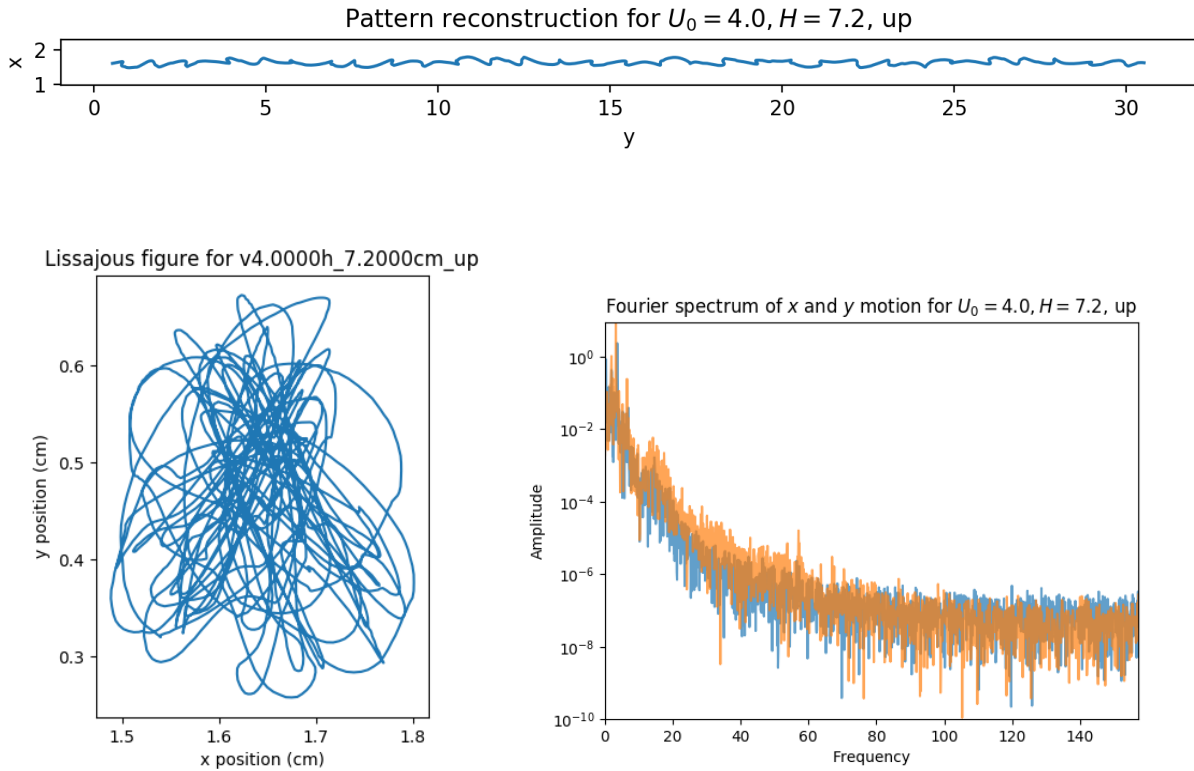
Figure 34: Disordered motion: pattern reconstruction, Lissajous plot, and frequency spectrum

Due to camera limitations–namely, the maximum number of frames to capture at a time being 3000–detailed analysis of the disordered motion, such as time-delay embedding, was not viable.

9 Challenges

9.1 Buckling

When buckling occurs, one section of the thread touches down on a point of the belt which differs from the point of contact, effectively creating a discontinuity in the point of contact of the thread with the belt. Previous simulations and models, such as the one in [10] have

not accounted for this effect. Nevertheless, it has been observed in several different regimes, especially where the motion of the thread is disordered.

An example of such buckling may be seen in Figure 35.

Figure 35: Buckling of thread causing discontinuity in position of point of contact

Buckling motion imposes a limitation on how close to the belt the position of the thread can be extracted from, since at certain heights above the belt, the thread position becomes multi-valued. Further investigation is necessary in order to better describe and account for this effect.

9.2 Air currents

At high heights, the thread has a relatively narrow diameter; this causes it to be very sensitive to the presence of air currents. These air currents cause the thread to 'wander' around the belt, making it more difficult to discern periodic motion from aperiodic motion. A plot with a state at a height affected by air currents is shown in Figure 36.

In an attempt to mitigate these air currents, a windbreaker was briefly installed, but it was found to have no discernible effect; hence, it was removed. However, there was no observable difference between the motion before and after the installation of a wind-breaking barrier. The motion of the belt itself is a likely cause for some of the air currents; thus, controlling for them entirely may not be practical.
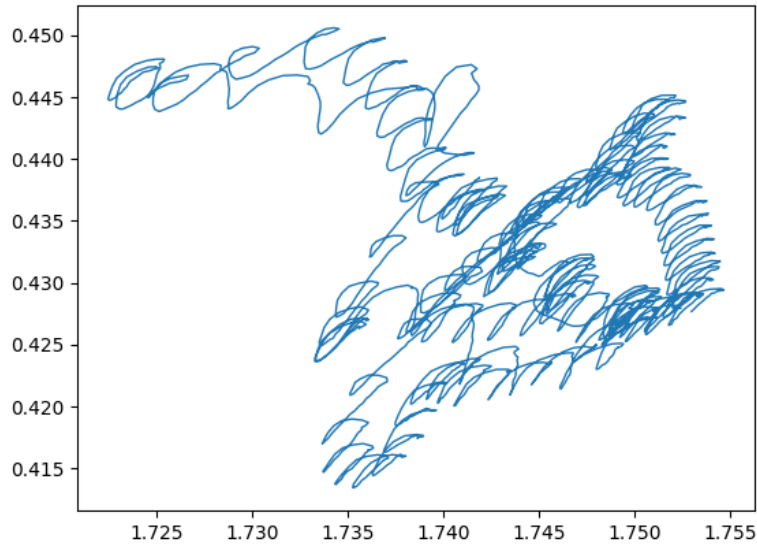
Figure 36: Example Lissajous plot of thread position affected by air currents

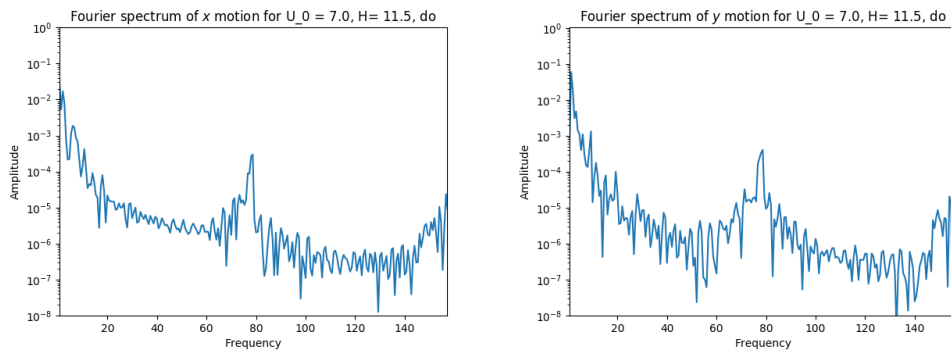The corresponding frequency spectra for the motion in Figure 36 may be found in Figure 37.

Figure 37: Frequency spectra of thread motion affected by air currents; note the relatively high magnitude of the low-frequency components.

10   Conclusion

Two related novel states of motion, here called 'loop kicks' and 'loop double kicks', were observed. Several states of motion with previously-uncharacterized frequencies were exam-

39

ined. Previously undocumented 'oscillatory double meandering' motion around the double meandering window was also observed and examined. More investigation is necessary to verify whether or not a pure double meandering state is present.

The frequency structure of side-kick motion was likewise examined, and found to be consistent with that of stretched coiling motion. Further investigation with more sensitivity to transverse thread motion is necessary in order to draw specific conclusions about whether or not side kick motion can be reproduced by the kinematic model.

Several windows of disordered motion states were observed; further investigation is necessary in order to verify whether or not these states are examples of chaotic motion. In particular, observing the behaviour of the disordered states over long time intervals would provide more insight into the characteristics of the motion.

Finally, another avenue for further investigation is examining the characteristics of the motion at higher heights, although careful development of a means to mitigate the effects of air currents is necessary.

References

[1] Neil M. Ribe. Coiling of viscous jets. *Proc. R. Soc. Lond.*, 460:3223–3239, 2004.

[2] N. M. Ribe, H. E. Huppert, M. a. Hallworth, M. Habibi, and Daniel Bonn. Multiple coexisting states of liquid rope coiling. *Journal of Fluid Mechanics*, 555:275, 2006.

[3] M. Maleki, M. Habibi, R. Golestanian, N. M. Ribe, and Daniel Bonn. Liquid rope coiling on a solid surface. *Physical Review Letters*, 93(21):19–22, 2004.

[4] Andrzej Herczyński, Claude Cernuschi, and L. Mahadevan. Painting with drops, jets, and sheets. *Physics Today*, 64(6):31–36, 2011.

[5] S. Chiu-Webster and J. R. Lister. The fall of a viscous thread onto a moving surface: a 'fluid-mechanical sewing machine'. *Journal of Fluid Mechanics*, 569:89–111, 2006.

[6] Xiaoqing Tian, Jeffery Plott, Hongjun Wang, Bizhong Zhu, and Albert J Shih. ScienceDirect Silicone Foam Additive Manufacturing by Liquid Rope Coiling. *Procedia CIRP*, 65:196–201, 2017.

[7] Tobias Luelf, Christian Bremer, and Matthias Wessling. Rope coiling spinning of curled and meandering hollow-fiber membranes. *Journal of Membrane Science*, 506:86–94, 2016.

[8] Stephen W. Morris, Jonathan H P Dawes, Neil M. Ribe, and John R. Lister. Meandering instability of a viscous thread. *Physical Review E - Statistical, Nonlinear, and Soft Matter Physics*, 77(6), 2008.

[9] Robert L. Welch, Billy Szeto, and Stephen W. Morris. Frequency structure of the nonlinear instability of a dragged viscous thread. *Physical Review E - Statistical, Nonlinear, and Soft Matter Physics*, 85(6), 2012.

[10] P Brun, N M Ribe, and B Audoly. A numerical investigation of the fluid mechanical sewing machine. *Physics of Fluids*, 24(4), 2012.

[11] 378429 Aldrich: Product specification.